# Near-Field Electron Energy Loss Spectroscopy of Nanoparticles

H. Cohen,[1] T. Maniv,[2] R. Tenne,[1] Y. Rosenfeld Hacohen,[1] O. Stephan,[3] and C. Colliex[3]

[1]*Weizmann Institute, Rehovot 76100, Israel*
[2]*Chemistry Department, Technion, Haifa 32000, Israel*
[3]*Physique des Solides, University of Paris-Sud, Orsay 91405, France*

Near-field spectroscopy of nanoparticles was performed with a subnanometer probe size, using a scanning transmission electron microscope. At nonintersecting beam-particle configuration, surface collective modes are isolated from the entire excitation spectrum. The relativistic narrow beam generates a new type of spatial dispersion and may induce an additional spectral quantization. Line intensity variations during the mapping can be accounted for quantitatively by using a relatively simple theoretical model. This method is also suggested as a new way for transmission electron microscopy studies of beam sensitive samples.　[S0031-9007(97)05029-1]

Recently, scanning transmission electron microscopes (STEM) equipped with analyzers for electron energy loss spectroscopy (EELS) achieved the combined capability of both high spatial resolution (below 1 nm) and energy resolution of several tenths of eV [1–9]. In typical EELS experiments, the scattering cross section includes contributions from the vacuum and within the solid, a fact that complicates considerably the spectrum interpretation. Separation of the surface excitations can, however, be achieved by using the TEM spatial capabilities at a configuration of no intersection between the beam and the detected solid. Such an experiment probes the electromagnetic near field of the sample, where the antenna, i.e., the *e* beam, is of a sub-nm size.

The proposed near-field EELS (NFEELS) is analogous to optical near-field spectroscopy, since the coupling between the "antenna" and the sample is dominated by the longitudinal field component. Commonly, transmission EELS theories use a classical particle description of the beam electrons [10], which cannot account properly for the transversal momentum distribution of the highly confined beam. Here, a quantum mechanical approach is chosen, incorporating the beam cross section and the sample size. Note that the experimental conditions greatly simplify the theoretical analysis: As long as the beam electrons propagate in the vacuum only, short range (impact) collision processes do not take place. Also, the first Born approximation is very well justified for electrons of typically 100 keV [11].

Measurements were performed on a VG STEM instrument (100 keV), fitted with a Gatan 666 parallel-EELS spectrometer [12]. The beam diameter was typically 5 Å and the energy resolution was 0.5 eV. An aperture of 6 mrad centered at the forward direction was used as the entrance to the energy analyzer, while a couple of high angle detectors (dark-field mode) enabled a simultaneous imaging. 2H-$MoS_2$ platelets were prepared using a gas-phase reaction between $MoO_{3-x}$ and $H_2S$ in a reducing atmosphere of $H_2(5\%)/N_2(95\%)$ at 950 °C [13]. Using a holey carbon grid (typical hole diameter 100 nm), isolated particles suspended by electrostatic forces into the vacuum could be selected for investigation. Hence, measurements were free of contributions from the support and the grid, yielding directly the loss spectrum of the desired objects. The atomically smooth and inert van der Waals surface of the platelet offered an ideally abrupt solid surface for investigation. Finally, by interacting from the vacuum, beam induced damage, mainly via excitation of core electrons, is practically eliminated.

A line scan across a representative $MoS_2$ platelet, approximately 100 nm high and 10 nm wide, is shown in Fig. 1. The spectra agree with the literature of bulk $MoS_2$. As the beam crosses the platelet surfaces, sharp spectral
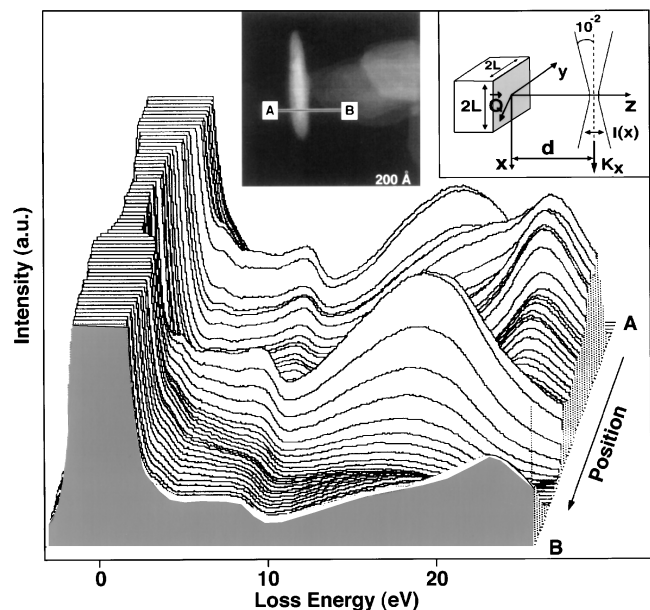


FIG. 1. A series of EEL spectra, recorded as the incident probe is rastered across a $MoS_2$ platelet. Left inset shows the image of the object and the path of the line scan (from *A* to *B*). Right inset illustrates the conical beam and the main scattering parameters.
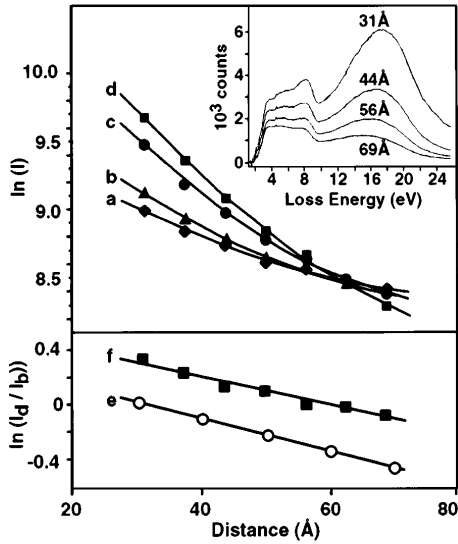
FIG. 2. Top: Evolution of line intensities (logarithmic scale) vs the beam-surface distance: the (a) 4.7, (b) 7.7, (c) 13.4, and (d) 16.6 eV modes. The inset shows several selected spectra, after removal of the elastic peak tail (beam-surface distances are noted). The small feature at 4.5 eV is an experimental artifact. Bottom: The intensity ratio of the 16.6 vs the 7.7 eV mode, manifesting the improvement of linear $d$ dependence: (e) calculated, without relativistic and beam size effects; (f) experimental data. Note that with a relativistic correction, the slope of curve $e$ reduces by a factor of $\sim 0.84$, leading to a close agreement with $f$.

changes are observed: the intensity of the zero loss peak (see variations in its width at the intensity cutoff) and the appearance/disappearance of the bulk plasmon around 23.2 eV. The maximal spatial broadening of the beam, estimated from the very first observation of bulk signal, is 25 Å, a value consistent with the expected broadening of the beam cone, along the entire platelet length. When the beam is restricted to the vacuum, the surface plasmon around 16 eV and some additional low-energy features are observed (at 3.3, 4.7, and 7.7 eV), exhibiting a pronounced intensity even at distances of 100 Å and above. Interestingly, along the line scan (Fig. 2, inset), modes of smaller energy become relatively more intense at large distances.

EELS low-energy lines are commonly ascribed to single-electron interband transitions. Although a number of works [11,14] pointed out that these features can be treated as additional plasmonic modes, this interpretation has not been widely accepted. The present results provide, for the first time, an experimental evidence for the plasmonic nature of all of the low-energy lines, a conclusion believed to be of a general validity: Their intensity is maximal right on the surfaces (both sides of the platelet), showing a roughly exponential decay into the vacuum and into the bulk [7]. A quantitative analysis of line intensities is presented in Fig. 2, based on decomposition into Gaussians, where second derivative spectra facilitated

the peak energies determination. Technically, 9 modes were required to get a high quality reproduction of the spectrum, reflecting fine spectral details which are seen in the derivative spectra only. Yet, once the decomposition of a single spectrum was optimized, positions and widths were kept constant for all subsequent pixels, leaving only 9 free parameters in the fit procedure. As demonstrated in Fig. 2, curves $a-d$, all of the extracted modes exhibit a similar decay vs distance, however, with slopes roughly proportional to the mode energy (see discussion below).

Considering only general kinematical aspects, the enhancement of low-energy surface modes at large distances can be understood from the analysis of the total momentum transfer, $q$. Within the first Born approximation $q \gtrsim k_i \Delta E / 2E_0$, where $k_i$ is the incident beam wave vector, $E_0$ is the incident beam kinetic energy, and $\Delta E$ is the loss energy. As beam coupling to the exponentially decaying amplitude of the surface plasmon is more efficient for small $q$ values, a relative enhancement of the low $\Delta E$ modes is expected at large distances.

In our model, the extremely narrow $e$ beam is described as a one-dimensional free electron wave, propagating along the $x$ axis, parallel to the $x$-$y$ face of the nanoparticle. We assume a rectangular shape for the platelet with squared ($x$-$y$) faces of size $2L$. In the $y$-$z$ directions, the beam is modeled by standing waves, confined within a "cavity," whose converging cross section obeys $l(x) = l_0 + 2\alpha|x|$, where $-L \leq x \leq L$. We also assume that the beam-surface distance $d$ is much smaller than $L$, so that translational invariance of the particle dielectric response may be assumed in the $x$-$y$ plane. A good quantum number in the experiment is the relativistic total energy of the incoming beam electron ($E$); hence, the longitudinal momentum depends on the quantum numbers $n_y, n_z = 1, 2, \ldots$ of the transverse (standing) waves. As $\alpha \ll 1$ and the energy of the transverse waves is much smaller than the longitudinal beam energy, the former energy levels can be calculated by using a Born-Oppenheimer-like separation of coordinates (transverse from longitudinal) and first order perturbation theory, to find $k_x^2 = (E/\hbar c)^2 - (mc/\hbar)^2 - \pi^2(n_y^2 + n_z^2)/\bar{l}^2$, where $\bar{l} \equiv \sqrt{l_0(l_0 + \alpha L)}$. Similarly, the total energy of the outgoing (scattered) beam is $E$-$\Delta E$, and its longitudinal momentum depends on the outgoing transverse quantum numbers $n_y', n_z'$, such that

$$\Delta k_x \equiv k_x - k_x' \approx (\Delta E/\hbar V) + (\hbar \pi/\bar{l})^2$$
$$\times (n_y'^2 - n_y^2 + n_z'^2 - n_z^2)Vc/2E, \quad (1)$$

where $V$ is the initial electron velocity.

Now, as long as the beam is restricted to the vacuum, it is coupled only to the surface charge distribution of the particle [15], and the inelastic scattering cross section is dominated by the excitation of surface plasmons. Within our model, this cross section is given by the formula

$$I(\omega, d) \propto \sum_{n_y, n_z=1}^{\infty} e^{-\beta E_{tr}(n_y, n_z)} \sum_{n_y', n_z'=1}^{\infty} D(\Delta k_x; n_y, n_z, n_y', n_z'; \omega)/[k_x(n_y, n_z)k_x'(n_y', n_z')], \quad (2)$$

where

$$D(\Delta k_x; n_y, n_z, n_y', n_z'; \omega, V) = \int_{-\infty}^{\infty} dq_x \int_{-\infty}^{\infty} dq_y \, \text{Im}[r(Q, \omega, V)] e^{-2\chi_1 d} |I_{12}(\Delta k_x - q_x; n_y, n_z, n_y', n_z'; Q)|^2 , \quad (2a)$$

$$I_{12} \equiv \frac{1}{2L} \int_{-L}^{L} e^{i(\Delta k_x - q_x)x} I_1(x; n_y, n_y', q_y)$$
$$\times I_2(x; n_z, n_z', Q) \, dx , \quad (2b)$$

with

$$I_1 \equiv \sum_{j=0}^{1} (-1)^j \{\text{sinc}[(k_y^j - q_y) l(x)/2]$$
$$+ \text{sinc}[(k_y^j + q_y) l(x)/2]\} l(x)/2 ;$$

$$I_2 \equiv \sum_{j=0}^{1} (-1)^j \text{Re}\{\text{sinch}[(Q + i k_z^j) l(x)/2]\} l(x) ;$$

$\text{sinc}(t) \equiv \sin(t)/t$; $\text{sinch}(t) \equiv \sinh(t)/t$; $Q \equiv \sqrt{q_x^2 + q_y^2}$; $k_{y,z}^j \equiv [n_{y,z} + (-1)^j n_{y,z}']\pi/l(x)$; and $\Delta E = \hbar\omega$ is the loss energy.

The integration in Eq. (2b) is limited to the dimensions of the platelet along the beam axis. This approximation is justified since the beam-particle interaction potential is strongly attenuated for $|x| > L$. In Eq. (2), the Gaussian distribution of the transverse energy levels, $E_{\text{tr}}(n_y, n_z) \equiv (\hbar\pi/\bar{l})^2 (n_y^2 + n_z^2)$, is introduced to take into account the initial conditions of the $e$ beam before its entrance into the scattering domain. This is a necessary step in our infinite potential barrier model, which artificially confines transversal waves with arbitrarily high quantum numbers $(n_y, n_z)$ within the "beam cavity." In the experiment, high transverse energy states are cut off from the beam by the objective aperture (before the entrance into the scattering domain). For the energy width parameter $1/\beta$, a value compatible with the spatial width parameter, $\bar{l}$, is used.

The response function in Eq. (2a) is given by [10]

$$r(Q, \omega, V) = [2\chi_1(\varepsilon - 1)/(\chi_1 \varepsilon + \chi_2)$$
$$- (1 - V^2/c^2)(\chi_1 - \chi_2)/\chi_1]/(\chi_1 + \chi_2) ,$$

where $\chi_1^2 \equiv Q^2 - (\omega/c)^2$; $\chi_2^2 \equiv Q^2 - (\omega/c)^2 \varepsilon(\omega)$; and a Drude-like dielectric function is taken, $\varepsilon(\omega) = 1 - \omega_p^2/(\omega^2 + i\omega\delta)$, where $\omega_p$ is the plasma frequency and $\delta$ is the damping parameter. Spatial dispersion of $\varepsilon$ is neglected here. The relativistic nature of the $e$ beam introduces, however, a strong $Q$ dispersion into the surface plasmon energy, determined by $\chi_1 \varepsilon(\omega) + \chi_2 = 0$. In the limit of infinite speed of light, the term $\exp[-2\chi_1 d] \text{Im}[r(Q, \omega, V)]$ reduces to the classical expression, yielding the lateral Fourier transform of the image potential [Eq. (2a)], $(\pi/Q) e^{-2Qd} \text{Im}[(\varepsilon - 1)/(\varepsilon + 1)]$.

The function $I_{12}$ [Eq. (2b)] reflects the relaxed condition of momentum conservation, associated with the finite size of the particle and the beam: In the limit when $L \to \infty$, $\alpha \to 0$, and $\alpha L < d$, $I_{12}$ is proportional to $\delta(\Delta k_x - q_x)$, yielding a full momentum conser-

vation along the longitudinal direction. The overall intensity retains then an almost pure exponential decay vs $d$, where the exponent is $2\chi_1$ (essentially proportional to $\Delta E$, see Eq. (1)]. Similar to the classical limit [10], $\omega/V = \Delta k_x$ in this case. For a finite particle size, $I_{12}$ is not anymore a $\delta$ function. Its nonvanishing tails allow a substantial contribution at $q_x \to 0$, associated with the long range nature of the Coulombic interaction term in $D$ [Eq. (2a)]. The distance $d$, which determines an effective window in $Q$ space, controls the balance between those two major contributions, the kinematical and the Coulombic one.

Another important effect on the intensity variations arises from the $Q$ dispersion $\omega(Q)$. The relativistic dispersion, for example, produces an energy band, typically with two distinct edges (compare curves $a$ and $b$, inset of Fig. 3). The low-energy edge corresponds to small $Q$ values [large exponential factors in Eq. (2a)] and low density of (plasmonic) states. At this energy, an almost strict linear $d$ dependence is predicted for the logarithm of line intensity. On the other hand, many small (and different) exponential factors contribute to a narrow energy interval around the second edge, resulting in an apparent nonlinear $d$ dependence. Hence, the relative weight of the
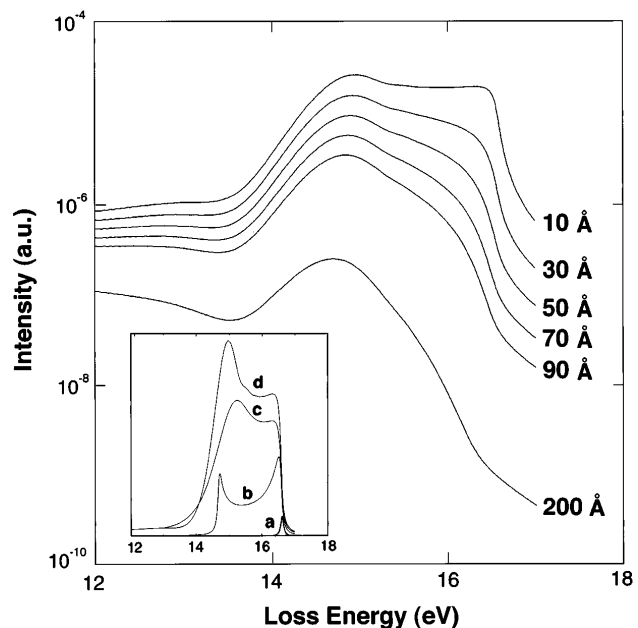


FIG. 3. Calculated scattering intensity $I(\omega)$, at several different distances, using a "single plasma" Drude-like dielectric function. The inset shows the calculated line shape (linear scale) for $d = 50$ Å, based on the different approximations (appropriately scaled for clarity): curve $a$, nonrelativistic; curve $b$, relativistic, with an infinite sample; curve $c$, a full calculation for a finite sample; curve $d$, like $c$, however, neglecting nonzero beam transverse momentum transfers.

two edges changes with $d$, leading to an overall impression of a line shift. This effect, believed to be already observed experimentally [16], is demonstrated in Fig. 3.

In general, quantum effects tend to smear the band edges, due to the uncertainty in momentum space. Curve $c$ in the inset of Fig. 3 exhibits the overall broadening expected from the experimental conditions, while curve $d$ isolates the effect of the finite particle size ($L = 1000$ Å). In fact, under appropriate conditions, the extremely small cross section of the beam can lead to an observable quantization, appearing as an additional fine structure superimposed on the dispersion curve. However, observation of this fine structure depends crucially upon the particle size: The variations of $l(x)$ along the $x$ direction should be smaller than $l_0$, i.e., $L \leq 100$ Å.

Analyzing the evolution of line intensities, one may start with the low-energy edge of the plasmon band, where a pure exponential decay is a good approximation. Indeed, our numerical calculations show that at 14.9 eV a good linear fit is obtained from $\ln(I)$ vs $d$, across a range of 200 Å. Deviations from the linear behavior can be estimated by writing $\ln(I) = A + Bd + Cd^2$, yielding for $d = 50$ Å: $Cd/B \approx 0.08$. The calculated slope, $B = 1.7 \times 10^{-3}\Delta E$, is 25% larger than $2\chi_1$ (for $q_y = 0$), the exponent extracted from classical considerations. Evidently, at the high-energy edge, where nonlinearity is inherently introduced by the relativistic effects, the intensity evolution is qualitatively different, and the parabolic correction increases to $Cd/B \approx 1$.

The above behavior is, in fact, limited to distances shorter than $\sim 1/\Delta k_x$ (the wavelength of the transmitted photon) and/or the particle size, $L$. For the sake of simplicity, we have studied the role of the particle size within a nonrelativistic framework, taking advantage of the fact that the $q_x \rightarrow 0$ contributions (*vide ultra*) do not depend on $\Delta E$. Indeed, the nonlinearity associated with the finite size of the particle is fully removed upon plotting intensity ratios of modes at different $\Delta E$ positions (curve $e$ in Fig. 2). Yet, for $d > 150$ Å (not shown in the figure), the linear behavior breaks down rapidly: The $q_x \rightarrow 0$ contributions become dominant, diminishing the dependence on mode energy, such that $\ln(I_1/I_2) \rightarrow 0$.

Our experimental results agree very well with the above predictions. All of the modes show a roughly exponential decay, with slopes $(1.65 \pm 0.2)10^{-3}\Delta E$ that lay within $(5-10)\%$ of the calculated value. The slope dependence on $\Delta E$ explains the remarkable observation that, at large distances, low-energy modes become even more intense than the main plasmon. A quadratic correction, $Cd/B \approx 0.25$ (at $d = 50$ Å), is common to all of the main modes. Moreover, by analyzing intensity ratios (compare curve $f$ with $a-d$, Fig. 2), the nonlinearity is reduced by a factor of $\sim 2$, in full agreement with the theoretical estimation of the particle size effect. Obviously, the existence of several overlapping surface modes does not permit the observation of fine details within the plasmonic band. Note that the

intrinsic dispersion of the dielectric function, neglected in our model, should further blur those details, as its high density of states corresponds to $Q \rightarrow 0$.

Finally, the surface plasmons contain significant information about the particle geometry on the nanometer length scale. A line scan performed along the $y$ axis towards the narrow edge of the same platelet, shows that long wavelength surface modes are extinguished due to the small thickness of the platelet, as expected when a particle side is reduced to the order of $1/\Delta k_x$.

In conclusion, NFEELS has been shown to probe effectively the electromagnetic near field of nanoparticles. Having a sub-nm probe size and an enhanced sensitivity to surface plasmons, it is complementary to optical near-field spectroscopies. A simple theoretical model provides an accurate reproduction of intensity profiles, with a considerable sensitivity to finite size effects. In addition, this technique may be applied to samples which are sensitive to the traditional TEM measurements.

[1] D. Bouchet, C. Colliex, P. Flora, O. Krivanek, C. Mory, and M. Tence, Microsc. Microanal. Microstruct. **1**, 443 (1990).

[2] R. F. Egerton, *EELS in the Electron Microscope* (Plenum, New York, 1986).

[3] J. Fink, Adv. Electron. Electron Phys. **75**, 121 (1989).

[4] D. A. Muller, W. Tsou, R. Raj, and J. Silcox, Nature (London) **366**, 725 (1993).

[5] P. E. Batson, Nature (London) **366**, 727 (1993).

[6] P. M. Ajayan, C. Colliex, J. M. Lambert, P. Bernier, L. Barbedette, M. Tence, and O. Stephan, Phys. Rev. Lett. **72**, 1722 (1994).

[7] P. E. Batson, Ultramicroscopy **11**, 299 (1983).

[8] M. Acheche, C. Colliex, H. Kohl, A. Nourtier, and P. Trebbia, Ultramicroscopy **20**, 99 (1986).

[9] D. Ugarte, C. Colliex, and P. Trebbia, Phys. Rev. B **45**, 4332 (1992).

[10] R. Garcia-Molina, A. Gras-Marti, A. Howie, and R. H. Ritchie, J. Phys. C **18**, 5335 (1985).

[11] H. Raether, in *Excitations of Plasmons and Interband Transitions by Electrons*, edited by G. Hohler, Springer Tracts in Modern Physics Vol. 88 (Springer-Verlag, Berlin, 1980).

[12] M. Tence, M. Quartuccio, and C. Colliex, Ultramicroscopy **58**, 42 (1995).

[13] Y. Feldman, E. Wasserman, D. J. Srolovitz, and R. Tenne, Science **267**, 222 (1995).

[14] H. Cohen, M. Folman, T. Maniv, R. Brener, E. Lifshitz, and Z. Esterlit, Phys. Rev. B **46**, 4446 (1992).

[15] T. Maniv and P. Gies, Surf. Sci. **211/212**, 242 (1989).

[16] P. Moreau, N. Brun, C. A. Walsh, C. Colliex, and A. Howie, Phys. Rev. B **56**, 6774 (1997).